The Impact of Tides on Simulated Landfast Ice in a Pan-Arctic Ice-Ocean Model

Jean-François Lemieux, Ji Lei, Frédéric Dupont, François Roy, Martin Losch, Camille Lique, Frédéric Laliberté

The Impact of Tides on Simulated Landfast Ice in a Pan-Arctic Ice-Ocean Model

Jean-François Lemieux[1] [ID], **Ji Lei[2]**, **Frédéric Dupont[2]** [ID], **François Roy[1]**, **Martin Losch[3]** [ID], **Camille Lique[4]** [ID], **and Frédéric Laliberté[5]** [ID]

[1]Recherche en Prévision Numérique Environnementale/Environnement et Changement Climatique Canada, Dorval, Québec, Canada, [2]Service Météorologique du Canada, Environnement et Changement Climatique Canada, Dorval, Québec, Canada, [3]Alfred-Wegener-Institut, Helmholtz-Zentrum für Polar- und Meeresforschung, Bremerhaven, Germany, [4]IFREMER, Univ. Brest, CNRS, IRD, LOPS, Plouzané, France, [5]Climate Research Division, Environment and Climate Change Canada, Toronto, Ontario, Canada

Abstract The impact of tides on the simulated landfast ice cover is investigated. Pan-Arctic simulations are conducted with an ice-ocean (CICE-NEMO) model with a modified rheology and a grounding scheme. The reference experiment (without tides) indicates there is an overestimation of the extent of landfast ice in regions of strong tides such as the Gulf of Boothia, Prince Regent Inlet, and Lancaster Sound. The addition of tides in the simulation clearly leads to a decrease of the extent of landfast ice in some tidally active regions. This numerical experiment with tides is more in line with observations of landfast ice in all the regions studied. Thermodynamics and changes in grounding cannot explain the lower landfast ice area when tidal forcing is included. We rather demonstrate that this decrease in the landfast ice extent is dynamically driven by the increase of the ocean-ice stress due to the tides.

Plain Language Summary Landfast ice is sea ice that is immobile near a coast for a certain period of time. This coastal ice can stay at rest because it is attached to the coast and/or anchored to the seafloor in shallow water. To study landfast ice, we used a numerical model that represents the physical interactions between the atmosphere, the ocean, and the sea ice. We compared two simulations done with this model: one without ocean tides and one that includes the tides. The experiment with tides exhibits a lower extent of landfast ice which is more in line with the observations. This decrease in the landfast ice extent when adding the tides is a dynamical process; the strong tidal currents constantly set the sea ice in motion, preventing it to become landfast.

1. Introduction

Immobile or almost immobile sea ice located near a coast is often referred to as landfast ice. Landfast ice is observed in many coastal regions of the Arctic (Yu et al., 2014) and of the Antarctic (Nihashi & Ohshima, 2015). In the Arctic (the region of interest in this paper), large extents (up to hundreds of kilometers into the sea) of landfast ice are observed in winter and spring in the East Siberian, the Laptev, and the Kara Seas. In the Laptev Sea, grounded pressure ridges have been observed and identified as anchor points for the stabilization of the landfast ice cover (Haas et al., 2005; Selyuzhenok et al., 2017). Modeling experiments suggest that grounding is also an important mechanism for the presence of landfast ice in the East Siberian Sea (Lemieux et al., 2016, 2015). As the Kara Sea is overall deeper than the East Siberian and Laptev Seas, grounding is less effective and it is thought that a series of islands act as pinning points for stabilizing its landfast ice cover (Divine et al., 2005; Olason, 2016). In the Chukchi and Beaufort Seas, where the continental shelves are narrower than in the East Siberian and Laptev Seas, the landfast ice cover can extend a few tens of kilometers away from the coast. Grounding is again an important physical process for explaining the presence of landfast ice in these regions (Mahoney et al., 2014, 2007). Landfast ice is also present off the east coast of Greenland, in some coastal regions of Baffin Bay and Hudson Bay and in many inlets and channels of the Canadian Arctic Archipelago (CAA) where the ice is landlocked.

Landfast ice has an important impact on ocean-ice-atmosphere interactions. Indeed, as it is immobile, it decreases the transfer of heat, moisture, and momentum between the atmosphere and the ocean. The off-shore edge of landfast ice often exhibits polynyas that can be important sites for the formation of new sea

ice (Dethleff et al., 1998). It has also been shown that the landfast ice cover off the Siberian shelf plays a role in the formation of the Arctic cold halocline layer (Itkin et al., 2015). The presence of landfast ice can, locally, strongly modulate the mean and the structure of the ocean flow through narrow straits such as Nares Strait (Rabe et al., 2012).

Due to their low spatial resolutions and the lack of representation of some physical mechanisms such as grounding, sea ice models usually poorly simulate the landfast ice cover (Johnson et al., 2012; Laliberté et al., 2018). With the increase in spatial resolution of ice-ocean forecasting systems and even of climate models, there is growing interest in better representing the formation, stabilization, and breakup of landfast ice. Hence, over the past few years, some modelers have modified the sea ice rheology and have developed parameterizations to better simulate landfast ice. Dumont et al. (2009) studied the impact of the ellipse aspect ratio of the standard viscous-plastic (VP) rheology on the simulation of the North Water Polynya ice bridge. In order to model landfast ice, König Beatty and Holland (2010) introduced a simple formulation for adding isotropic tensile strength to the standard VP rheology. Itkin et al. (2015) increased the ice strength in shallow regions in order to better simulate landfast ice. Olason (2016) studied the impact of some physical and numerical parameters of a VP model on the simulated landfast ice in the Kara Sea. Rallabandi et al. (2017) developed an analytical theory of the flow of sea ice through narrow straits and on the formation of ice bridges. Dansereau et al. (2017) investigated the simulation of ice bridges with the new Maxwell-elasto-brittle rheology. To represent grounding in shallow water, Lieser (2004) proposed a simple approach to set the ice at rest. Following the work of Lieser (2004), Lemieux et al. (2015) introduced a parameterization that represents the seabed (or basal) stress in the momentum equation due to grounded ice ridges.

Recently, it was shown that landfast ice in the Arctic can be reasonably well simulated by using a grounding scheme and a modified VP rheology (Lemieux et al., 2016). However, Figure 8 in Lemieux et al. (2016) indicates that the model clearly overestimates the presence of landfast ice in the Gulf of Boothia, Prince Regent Inlet, Lancaster Sound and to a lesser extent in Foxe Basin. Interestingly, these regions are known to experience strong tidal forcing. As tides were not included in the ice-ocean simulations of Lemieux et al. (2016), this overestimation could be due to the absence of this forcing.

Tides are, in general, of small amplitude in the Arctic. They can be significant in many regions in Canadian waters (as mentioned above) and in regions such as the White Sea and the Barents Sea. In the latter region, tides are an important source of energy dissipation and control part of the heat loss from the Atlantic Water to the atmosphere and the dense water formation (Årthun et al., 2011). These water mass transformations are important as they might determine the location of the ice edge. Observations show that enhanced turbulent mixing due to tides is associated with rough topography (Rippeth et al., 2015). Tidal motion also has a direct dynamical impact on sea ice as it generates divergence-convergence cycles that affect the sea ice growth and melting (Koentopp et al., 2005). Holloway and Proshutinsky (2007) also discuss this competition between a more important melt due to enhanced ocean heat fluxes and more absorption of solar radiation in summertime leads and larger ice growth due to the rapid openings and closings of leads. Tides are also thought to play a role in the formation and maintenance of some Arctic polynyas (Hannah et al., 2009).

In this paper, we will show that including tides notably decreases the simulated area of landfast ice in regions such as the Gulf of Boothia, Prince Regent Inlet, Lancaster Sound, Nares Strait, and Foxe Basin. The objectives are to study the impact of tides on the simulated landfast ice (not the opposite) and to identify the mechanisms that lead to such a lower extended landfast ice cover in these regions. See, for example, Kowalik and Proshutinsky (1994) for a discussion on the influence of landfast ice on tides. Some authors have studied the impact of tides on the simulated pack ice (e.g., Årthun et al., 2011; Holloway & Proshutinsky, 2007; Koentopp et al., 2005; Kowalik & Proshutinsky, 1994; Luneva et al., 2015), but it is, to our knowledge, the first time that a numerical study focuses on the influence of tides on landfast ice.

This paper is structured as follow. In section 2, the ice-ocean model is introduced and the experimental setup is described. Some model validations are shown in section 3. Observations and the methodology used for this study are presented in section 4. The main results are presented in section 5. Concluding remarks are provided in section 6.
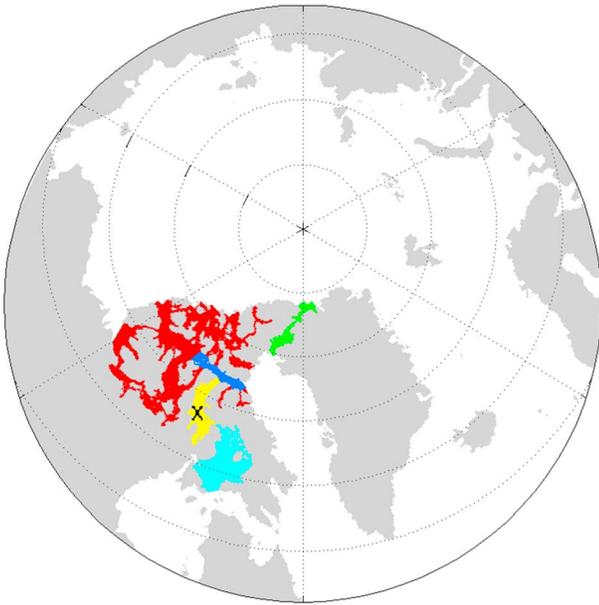
Figure 1. Part of the domain analyzed. Four regions with strong tides are defined and respectively referred to as Nares in green, Lancaster in blue, Boothia in yellow, and Foxe Basin in cyan. An additional region, where the impact of tides on the landfast ice cover is less important, is referred to as the *rest of the Canadian Arctic Archipelago* in red. The black cross identifies a point in the Gulf of Boothia used as a site for time series. In this paper, we refer to subregions Nares, Lancaster, Boothia, and Foxe Basin as the tidally active regions.
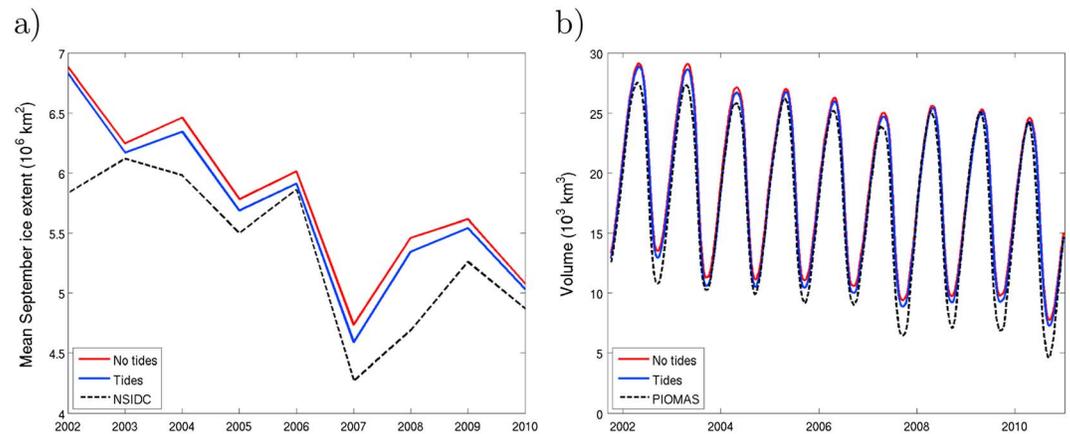
2. Experimental Setup

A pan-Arctic ice-ocean model is used to conduct two 10-year simulations (1 October 2001 to 31 December 2010): one with *no tides*, referred to as NT, and one with *tides*, referred to as T. The sea ice model is CICE version 4.0 (Hunke & Lipscomb, 2008) with some modifications that include the UK Met Office CICE-NEMO interface (Megann et al., 2014), the grounding scheme of Lemieux et al. (2015), and a modified VP rheology as described in Lemieux et al. (2016). Including the seabed stress as in Lemieux et al. (2016), the sea ice momentum equation becomes

$$m\frac{D\mathbf{u}_i}{Dt} = -\mathbf{k} \times mf\mathbf{u}_i + \tau_a + \tau_o + \tau_b + \nabla \cdot \sigma - mg\nabla H_o, \tag{1}$$

where m is the combined mass of ice and snow per unit area; $\frac{D}{Dt}$ is the total derivative; t is the time; f is the Coriolis parameter; $\mathbf{u}_i = u_i\mathbf{i} + v_i\mathbf{j}$ is the horizontal sea ice velocity vector; $\mathbf{i}$, $\mathbf{j}$, and $\mathbf{k}$ are unit vectors aligned with the x, y, and z axis of the coordinate system; $\tau_a = \tau_{ax}\mathbf{i} + \tau_{ay}\mathbf{j}$ is the atmospheric stress; $\tau_o = \tau_{ox}\mathbf{i} + \tau_{oy}\mathbf{j}$ is the ocean stress; $\tau_b = \tau_{bx}\mathbf{i} + \tau_{by}\mathbf{j}$ is the seabed (or basal) stress term due to grounded ridges; $\nabla \cdot \sigma$ is referred to as the rheology term with σ the internal ice stress tensor with components given by $\sigma_{11} = \sigma_{xx}$, $\sigma_{22} = \sigma_{yy}$, and $\sigma_{12} = \sigma_{xy}$; g is the gravity; and H_o the sea surface height. In CICE, the advection of momentum is neglected. In our model implementation, the stresses τ_a and τ_o are formulated as in Roy et al. (2015).

CICE is based on a VP rheology with an elliptical yield curve (Hibler, 1979). To improve the simulation of landfast ice, the standard VP rheology is modified by setting the ellipse aspect ratio to 1.4 and by adding a small amount of isotropic tensile strength (k_t=0.05; Lemieux et al., 2016). The basal stress parameters for the grounding scheme are the same as in Lemieux et al. (2016), that is, k_1=8 and k_2 =15 Nm^{-3}. The momentum equation is solved with the Elastic-VP approach (Hunke, 2001). For a better numerical convergence of the Elastic-VP solver, we used a larger number (920) of subcycling iterations than the default value (120). CICE uses an ice thickness distribution model, here with 10 thickness categories (as defined in ; Smith et al., 2016). The advective time step Δt is 10 min.

The ocean model is NEMO version 3.6 (Madec, 2008) applied in a variable volume and nonlinear free surface configuration (with some modifications for the tides as explained below). Ocean mixing is parameterized with the NEMO TKE scheme. Seventy-five vertical ocean levels are used. As for the sea ice model, the ocean time step is 10 min.

Our 0.25° grid covers the Arctic, the North Atlantic, and the North Pacific (it is an extended version of the grid used by Lemieux et al., 2016, which did not include the Pacific portion). This subset of the 0.25° global ORCA mesh has a spatial resolution of ~12.5 km in the central Arctic. We focus on the Arctic Ocean and Canadian waters (see Figure 1 for the region of interest).

The ice-ocean simulations are forced by 33-km resolution atmospheric reforecasts from Environment and Climate Change Canada (Smith et al., 2014). The simulations were initialized with average (September–October 2001) sea ice concentration from the National Snow and Ice Data Center (NSIDC, https://nsidc.org/data/seaice_index/) and the average (October-November 2003) sea ice thickness field derived from ICESat data (https://nsidc.org/data/icesat). Initial conditions for the ocean temperature and salinity are derived from averages (September–October) of WOA13_95A4 fields (Locarnini et al., 2013; Zweng et al., 2013). The ocean starts at rest (with the sea surface height field and currents set to zero).

For the two open boundaries (North Pacific and North Atlantic), a monthly averaged circulation taken from the GLORYS2 version 4 reanalysis (Garric et al., 2017), providing vertical profiles of ocean currents, temperature, and salinity is applied. The nonlinear free surface (including the tides) is treated following a time-splitting technique with a sub–time step of 20 s. Vertically averaged velocities (13 harmonic components) were extracted from the solution of the Oregon State University (OSU) tidal prediction model (Egbert & Erofeeva, 2002). For

Figure 2. September mean sea ice extent as a function of the year for NT (in red), T (in blue), and the National Snow and Ice Data Center (NSIDC) data (in dashed black; a). The extent is defined as the surface inside the 15% concentration contour line. Daily sea ice volume as a function of time for NT (in red), T (in blue), and from the Pan-Arctic Ice Ocean Modeling and Assimilation System (PIOMAS) Arctic sea ice volume reanalysis (b).

the open boundaries the barotropic velocity components are prescribed as in Flather (1976). The tidal potential over the model domain is also considered as a sea surface height forcing term, including a correction for the self-attraction and loading effect.

The fact that the Environment and Climate Change Canada atmospheric forcing data set starts in 2001 and that the landfast ice data set (National Ice Center, 2006, updated 2009) used for our study ends in 2007 puts some constraints on the spinup period and the main analysis period. To improve the spinup, an initial pseudo-spinup is conducted by performing the first year (1 October 2001 to 30 September 2002) three times. After these 3 years of simulation, CICE-NEMO is restarted on 1 October 2001 and ran until 31 December 2010. This procedure is done for both T and NT simulations. The period from October 2001 to September 2004 is considered as the final spinup of the simulations while the rest (until 31 December 2010) is used for the analyses.

The 0.25° resolution CICE-NEMO configuration used for this paper is a testing platform for our 1/12° short-term regional ice ocean prediction system (RIOPS) now running operationally. When implementing the tides in RIOPS, we noticed that the sea ice thickness field exhibited unrealistic values (more than 10 m) at the end of the growth season in some tidally active regions. Our investigation pointed out that the ice was too weak in these regions when using the ice strength parameterization of Rothrock (1975; with modifications by Lipscomb et al., 2007). This problem was mitigated by using the ice strength parameterization of Hibler (1979). This result is in a sense consistent with the study of Ungermann et al. (2017) who showed that pan-Arctic ice-ocean simulations are closer to observations when using the formulation of Hibler (1979) rather than the one of Rothrock (1975). Hence, for the experiments described in this paper, the Hibler parameterization was used with the ice strength parameter ($P*$) equal to the widely used value of 27.5 $\times 10^3$ Nm^{-2}. The other CICE physical parameters are set to the default values (Hunke & Lipscomb, 2008).

3. Model Validation

Our CICE-NEMO model has been extensively tested and validated in both global (Roy et al., 2015) and regional (Lemieux et al., 2016) configurations. With the recent addition of tides and the switch from NEMO version 3.1 to version 3.6, the quality of the model simulations was re-examined. Some of these model validations are presented in Figures 2 and 3.

Except at the beginning of the time series, the simulated mean September sea ice extents for NT and T show behaviors very close to the one of the NSIDC observations (Figure 2a). The two time series exhibit slightly larger extents than the NSIDC data but with downward trends similar to the observations. The 2007 minimum is also quite well captured by the simulations. Consistent with the results of Luneva et al. (2015), the time series of the simulated total sea ice volume indicate that NT has slightly more volume than T (especially true in summer; Figure 2b). The NT and T simulations tend to have more volume than the Pan-Arctic Ice Ocean
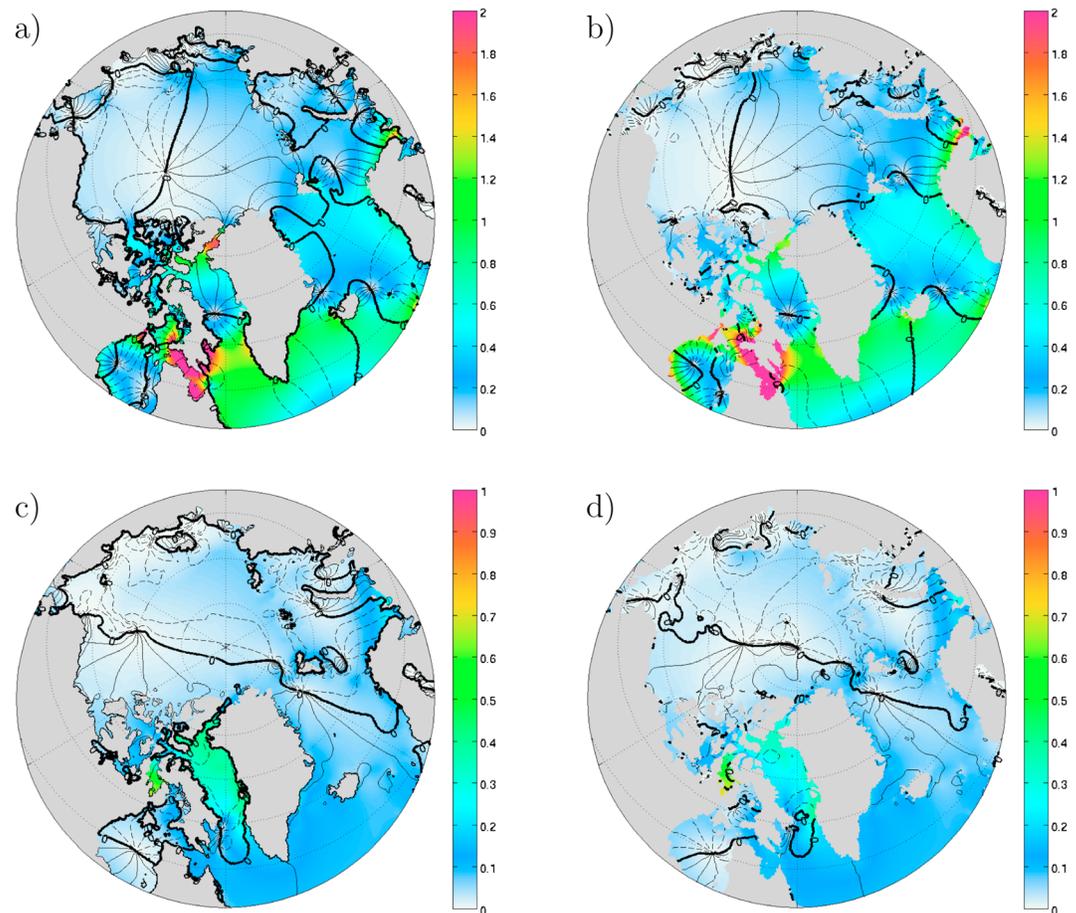
Figure 3. Amplitude (m) and phase of the simulated (a) and OSU reconstructed (b) tidal harmonic M2. Amplitude (m) and phase of the simulated (c) and OSU reconstructed (d) tidal harmonic K1. OSU = Oregon State University.

Modeling and Assimilation System (PIOMAS) sea ice volume reanalysis (Schweiger et al., 2011) especially at the end of the melt season (more notable in 2007 and onward). The three time series exhibit comparable downward trends. This kind of comparison with the PIOMAS volume time series should be taken with a grain of salt as PIOMAS is also an ice-ocean model (Zhang & Rothrock, 2003) that does not assimilate any sea ice thickness data (although it assimilates ice concentration and sea surface temperature).

Figure 3 compares the simulated and OSU reconstructed amplitude and phase for the two most important harmonics (M2 and K1). Three hundred days was used for the harmonic analysis. In the regions shown in this figure that can exhibit an ice cover, these harmonics exhibit large amplitudes in the White Sea, Nares Strait, and in Canadian waters (e.g., Foxe Basin and Hudson Strait). For both harmonics, the spatial pattern of the simulation is very similar to the OSU one. However, the amplitude of the simulated M2 harmonic is usually underestimates compared to OSU (with a notable exception in Nares Strait). The simulated tides are not perfect, but we consider they are reasonable for this study.

4. Description of Observations and Methodology

The National Ice Center (NIC) 25-km-gridded landfast ice product (National Ice Center, 2006, updated 2009) is used for validation. These bi-weekly pan-Arctic analyses, manually produced, identify grid cells that are covered by landfast ice. To compare the simulations to the NIC analyses, we follow most of the methodology of Lemieux et al. (2016). Hence, the NIC landfast ice observations are interpolated to the model grid by doing a nearest grid point interpolation.

Event though our simulations end on 31 December 2010, we focus on the period from September 2004 to September 2007 because the NIC landfast ice data ends in 2007. For the simulations, daily averaged gridded
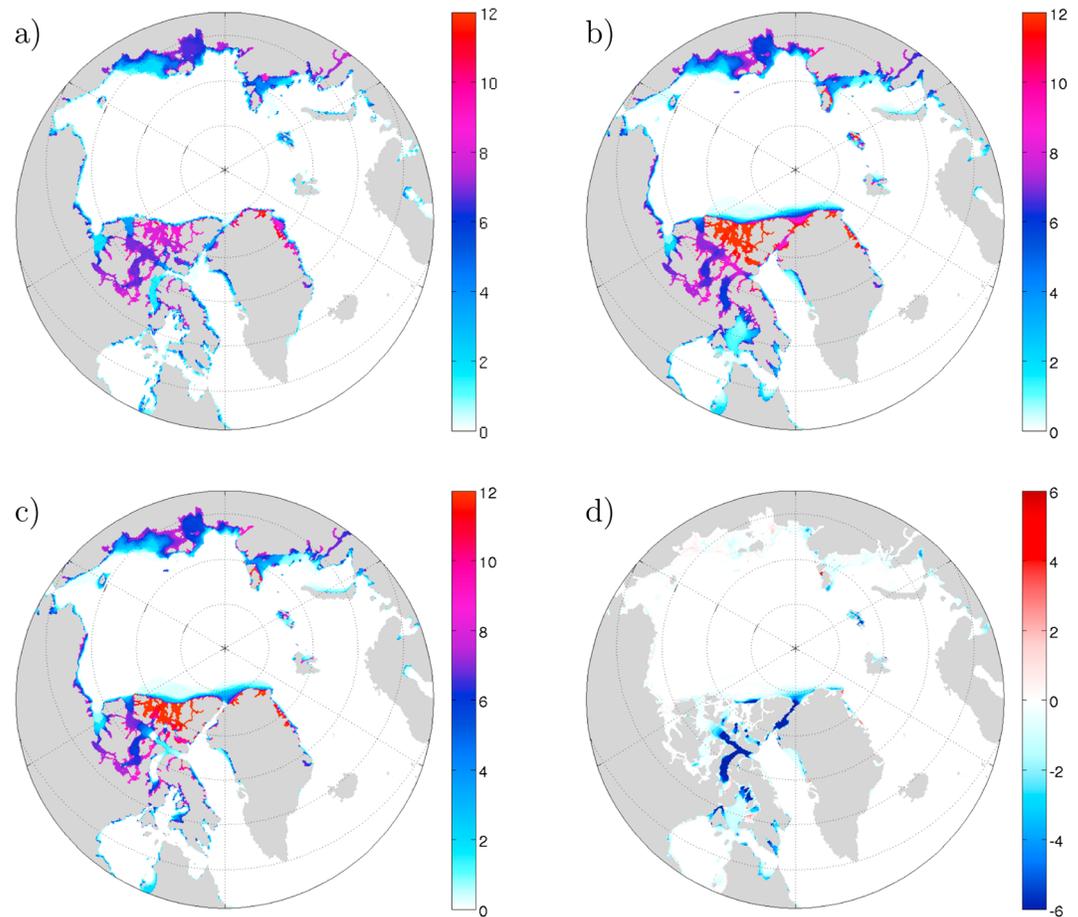
Figure 4. Average number of months of landfast ice, for the period September 2004 to September 2007, for the observations (a), for the NT simulation (b), and for the T simulation (c). The last panel (d) shows the difference between the number of months of landfast ice for the T simulation minus the number of months for the NT one ($N_T - N_{NT}$).

outputs (defined at the tracer point) are saved. Simulated ice at a certain grid cell is considered landfast if its 2-week mean daily speed is smaller than 5×10^{-4} m/s (as done in ; Lemieux et al., 2015). The area of landfast ice in a particular region is calculated by summing the area of landfast cells. Subregions (shown in Figure 1) are used to characterize the effect of tides on landfast ice in specific geographical areas. We also use the daily outputs to calculate the mean (of various variables) at each grid cell between January and May for the 3-year period (September 2004 to September 2007), in order to concentrate on the core of the landfast ice season.

To have a better understanding of the impact of high-frequency forcing (i.e., the tides) on the sea ice cover, hourly outputs are also saved and analyzed for a shorter period (20 October 2005 to 15 June 2006). Using these outputs, we choose a point in the middle of the Gulf of Boothia and compare the T and NT simulations.

5. Results

Following Laliberté et al. (2018), we calculated the average number of months of landfast ice (per year) at each grid point for the NIC observations (N_{obs}) and the simulations (N_T and N_{NT}). Figure 4a shows the number of months per year of landfast ice based on the NIC analyses (N_{obs}). Similarly, the number of months for the NT simulation (b) and the T simulation (c) are also displayed. The last panel (d) of this figure is the difference between the T and NT simulations (i.e., $N_T - N_{NT}$).

The number of months of landfast ice in the NT simulation is close to the number of months in the NIC analyses in coastal regions of the Arctic Ocean and in the Western part of the CAA. However, the NT simulation clearly overestimates the duration of landfast ice in the northern part of the CAA and in tidally active regions. In the northern CAA, the overestimation is due to the fact that some landfast ice survives the whole summer.

Table 1
Mean Error of the Number of Months of Landfast Ice for Different Subregions for the NT and T Simulations

Region	NT	T
Nares Strait	5.25	3.41
Lancaster	3.63	2.67
Boothia	3.91	2.06
Foxe Basin	2.03	1.01
rest of CAA	1.80	1.73
All regions	2.34	1.76

Note that multiyear landfast ice is rare but is sometimes observed in some channels of the CAA (e.g., Sverdrup channel; Serson, 1974). In regions such as the Gulf of Boothia, Prince Regent Inlet, and Lancaster Sound, however, the reason for the overestimation of the number of months in the NT simulation is different. Indeed, in these tidally active regions, the NT simulation exhibits an extended landfast ice cover in winter and spring while this is not observed.

Compared to the NT simulation, the number of months of landfast ice is notably reduced in the T simulation in the regions of strong tides. This suggests that, to the first order, the impact of tides on the landfast ice cover is local. For most of these tidally active regions, including the tides improves the simulation of landfast ice. Nevertheless, although the landfast ice is better simulated in Lancaster Sound when including the tides, there is too little landfast ice in Barrow Strait. There is even a double-arch feature in Barrow Strait (Figure 4c) that is not present in the NIC analyses (Figure 4a). A few small polynyas (e.g., in Penny Strait) can be seen in the T simulation while they are not present in the NT one (Figure 4; see also Figure 9).

Including the tides also has a strong impact in Nares Strait where the NT simulation overestimates the number of months of landfast ice while the T simulation leads to an underestimation. In fact, the ice bridge does not form anymore when the tides are included. As the largest differences between the NT and T simulations are found in tidally active regions in Canadian waters and in Nares Strait, we will pay a particular attention to these regions.

To quantify if the tides overall improve the simulation of landfast ice, we have first defined four subregions (shown in Figure 1) based on the largest negative differences in Figure 4d (by visual inspection). We refer here to these subregions as the tidally active regions. An additional subregion (rest of CAA), where the differences are smaller, is also defined. We then calculated, for these subregions, the mean error defined as $\mathcal{E} = \frac{1}{S_{tot}} \sum_{i=1}^{n} \left| N_s^i - N_{obs}^i \right| S^i$ where the summation is performed over the n ocean cells of a given subregion, the superscript i refers to these ocean cells, S^i is the surface area of the ocean cell i, S_{tot} is the total ocean area of the subregion, and N_s is either N_{NT} or N_T. Table 1 gives the mean error results for the different subregions. The T simulation exhibits notable improvements in the number of months of landfast ice simulated in all the subregions. The improvement is particularly remarkable in the Boothia subregion (in yellow in Figure 1) as the mean error $\mathcal{E}$ drops from 3.91 months in the NT simulation to 2.06 months when including the tides.

To further illustrate the impact of the tides, Figure 5 shows the area of landfast ice in the tidally active region Boothia (in yellow in Figure 1). Six years of simulations are shown (September 2004 -September 2010) along with the NIC observations from September 2004 to the last analysis available (31 December 2007). The NT simulation clearly overestimates the area of landfast ice compared to the NIC analyses. Also, the landfast area for the NT simulation saturates at the end of each landfast ice season. This is due to the fact that, inconsistent with observations, region Boothia is fully covered with landfast ice. In contrast, the T simulation does not have region Boothia fully covered by landfast ice, which is more in line with the observations.
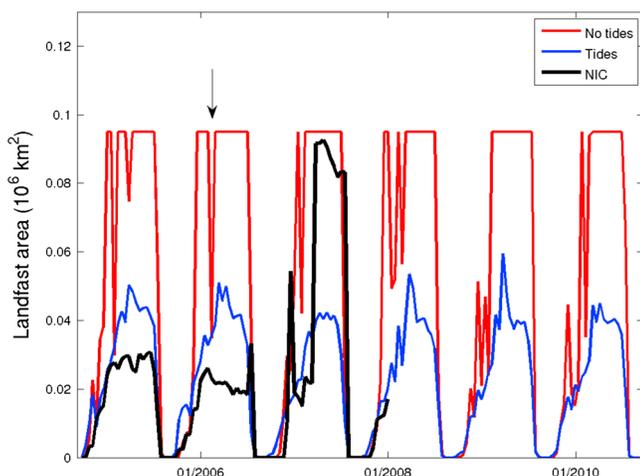
Figure 5. Area of landfast ice in the Boothia region (in yellow in Figure 1) as a function of time for the NT simulation (red), the T simulation (blue), and the NIC data (black). The black arrow indicates a breaking event in the NT simulation that will be discussed. Note that the NIC data end on 31 December 2007. NIC = National Ice Center.
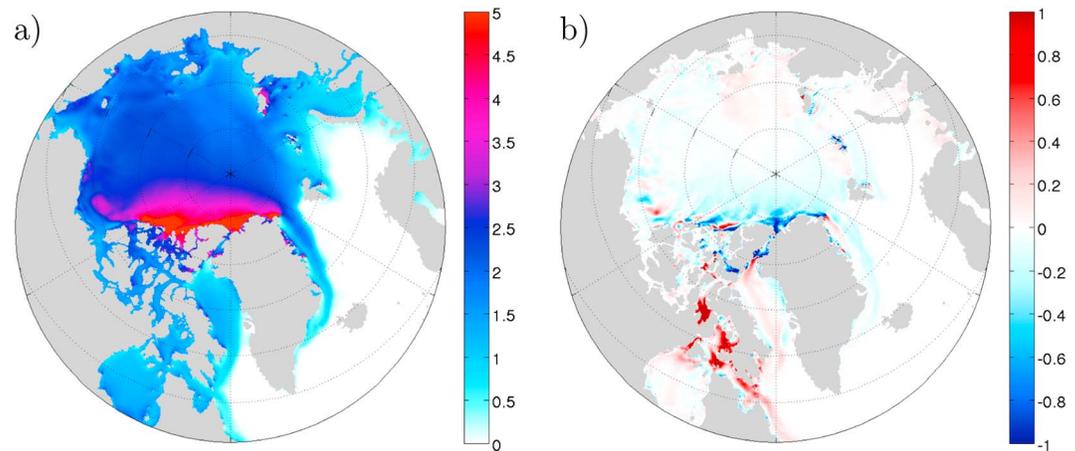
Figure 6. January–May mean (for the period September 2004 to September 2007) sea ice thickness (m) for the NT simulation (a). T-NT sea ice thickness (b).

There is, however, an increase in the observed landfast ice area at the end of March 2007. The landfast ice cover stays quite extended up to the end of the landfast ice season. This is not captured by the T simulation. This is, however, exceptional for the observed landfast ice extent in this region. Indeed, over the last 10 years of observations (1997–2007), it is the only period with such an extended landfast ice cover in this region (not shown).

To understand what causes the overall lower presence of landfast ice in the T simulations compared to the NT one, we investigate the changes in sea ice conditions, in grounding and in the forcing. We also examine whether the reduction in landfast ice when including the tides is dynamically and/or thermodynamically driven.

First, in Figure 6, we look at the differences in the ice volume per m^2 (in other words the mean thickness in a grid cell, simply referred to as the thickness). The thickness field is the January–May mean (for the period September 2004 to September 2007). Over most of the Arctic Ocean, the thickness fields are similar in the T and NT simulations. However, north of the CAA and Greenland, the ice is usually thinner in T than in NT. This could be due to the fact that the ice bridge does not form in T, which leads to more export of thick ice through Nares Strait (this is beyond the scope of this paper and would require a more thorough investigation). There are also large differences between the T and NT simulations in the southern Gulf of Boothia, the southern part of Foxe Basin, and in Hudson Strait (Figure 6b). Overall, in these tidally active regions, the ice is clearly thicker in the T simulation.

As the ice is thicker in the T simulation (in tidally active regions), this might suggest that grounding is more effective. This would, however, contradict the lower extent of landfast ice in the T simulation in the tidally active region. Figure 7a shows the magnitude of the basal stress (associated with grounding; Lemieux et al., 2015) for the NT simulation. This figure indicates that grounding is an important mechanism mainly along the Russian and Alaskan coasts. Because Nares Strait and most channels of the CAA are relatively deep, grounding is not an important process in these regions. Apart from the eastern part of Foxe Basin where the increase in grounding in the T simulation is obvious, the other regions of the CAA show no increase (too deep) or a small increase of the basal stress due to an overall thicker ice cover (Figure 7b). Hence, changes in grounding can certainly not explain the lower extent of landfast ice in the T simulation compared to the NT one; in fact, the slight increase in grounding in the T simulation should favor the formation/stabilization of landfast ice.

The fact that the ice is overall thicker in tidally active regions in the T simulation (Figure 6b) indicates that the ice cover is more active and leads to more ice production. This can be seen in the January–May mean (absolute) divergence of the sea ice velocity ($|\nabla \cdot \mathbf{u}_i|$; Figure 8) and in the January–May mean ice concentration (Figure 9). The large extents of landfast ice (Russian Coast and CAA) are clearly visible in the absolute divergence field of the NT simulation (Figure 8a). Figure 8b (T-NT) indicates that the ice is indeed more active in regions with strong tides in the CAA, Nares Strait, Foxe Basin, and Hudson Strait. Note that the difference between the T and NT mean absolute divergence fields can be expected to be larger if higher-frequency outputs were used, instead of daily means. Monthly mean spatial averages of the thermodynamic ice growth (not
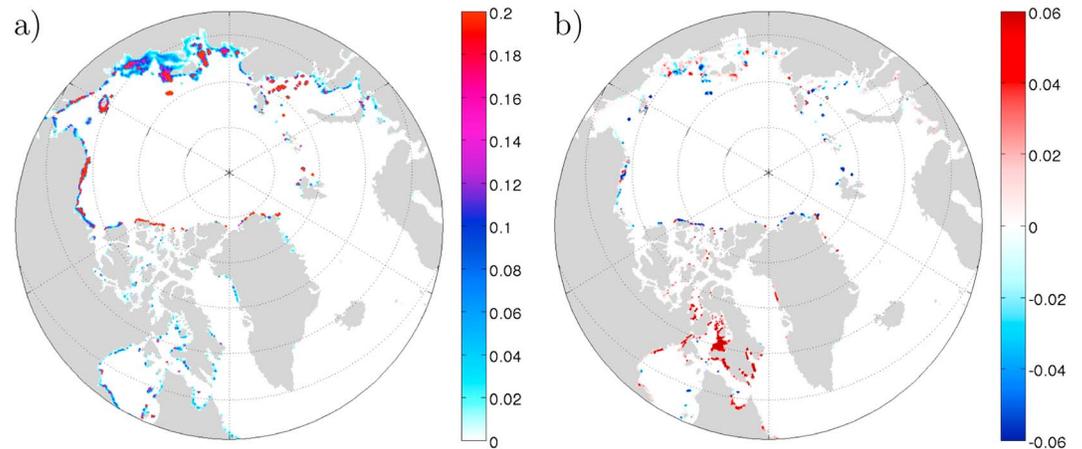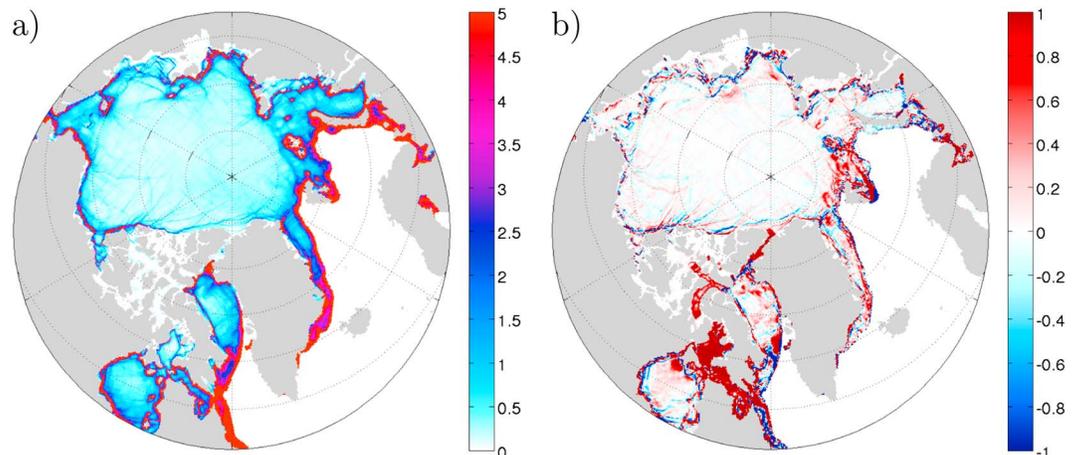
Figure 7. January–May mean (for the period September 2004 to September 2007) of the magnitude of the basal stress (Nm^{-2}) for the NT simulation (a). T-NT basal stress (b).

shown) exhibit a similar qualitative behavior for the four tidally active subregions: there is more growth in the T simulation than in the NT one during the growth season, because the more mobile ice creates more open water. The larger growth in T compared to NT in all these subregions is an integrated result; this is not true at all the points of these subregions. For example, the southernmost part of the Boothia region in the T simulation exhibits thicker ice, a slightly larger number of months of landfast ice and less thermodynamical growth than in the NT simulation.

As the ice strength based on Hibler's parameterization strongly decreases with the ice concentration, the ice strength is overall reduced in most of the tidally active regions (not shown) because the ice is overall less compact (Figure 9). Two exceptions are the southern Gulf of Boothia and the southern part of Foxe Basin. The increase in the ice strength in these regions is associated with thicker sea ice (Figure 6) and compact ice conditions (Figure 9).

We claim that the lower extent of landfast ice in the T simulation (in tidally active regions) is largely dynamically driven by the ocean stress at the ice interface (i.e., the ocean-ice stress simply referred to as the ocean stress in this paper). Although the difference (T − NT) of the mean (January–May) amplitude of the ocean stress clearly indicates it is larger in T than in NT in tidally active regions (not shown), a more interesting and complete view of the impact of the tidal forcing on the sea ice cover is provided by calculating the rate of change of sea ice kinetic energy (KE) per unit area.

Figure 8. January–May mean (for the period September 2004 to September 2007) absolute divergence of the sea ice velocity ($|\nabla \cdot \mathbf{u}_i|$, in day^{-1}) for the NT simulation (a). T-NT absolute divergence (b). Note that these fields were calculated where the January-May mean ice concentration was higher than 0.5. Absolute divergence values close to zero in ice covered regions indicate the presence of landfast ice.
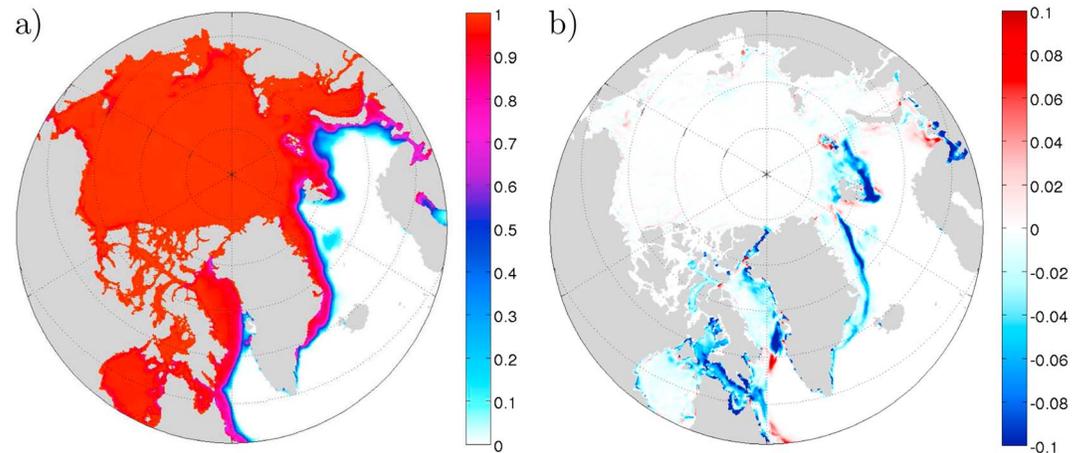
Figure 9. January–May mean (for the period September 2004 to September 2007) sea ice concentration for the NT simulation (a). T-NT sea ice concentration (b).

Following Bouchat and Tremblay (2014), we computed the scalar product of the ice velocity vector and the different terms in the momentum equation (equation (1)). Figure 10 shows the January–May 2006 mean rate of change of sea ice KE due to the atmospheric stress ($E_{ai} = \mathbf{u}_i \cdot \boldsymbol{\tau}_a$), the ocean stress ($E_{oi} = \mathbf{u}_i \cdot \boldsymbol{\tau}_o$), and the rheology term ($E_r = \mathbf{u}_i \cdot [\nabla \cdot \boldsymbol{\sigma}]$). In the NT simulation, the ocean stress (Figure 10c) and the rheology term (Figure 10e) dissipate KE almost everywhere in the domain, the KE input being provided by the wind stress term (Figure 10a). The regions of landfast ice are easily recognizable with values of E_{ai}, E_{oi}, and E_r close to 0 W/m². As the state of stress is in the viscous regime when the ice is landfast, the very small E_r in these regions is consistent with the conclusions of Bouchat and Tremblay (2014), that is, that the KE dissipated by the viscous regime is small and represents a negligible fraction of the total KE dissipated. Over most of the domain, E_{oi} and E_r in the T simulation (Figures 10d and 10f) are similar to the ones of the NT simulation. However, in regions of strong tides, the differences between the T and NT simulations are striking. In Foxe Basin, Nares Strait, the Gulf of Boothia, and Prince Regent Inlet, the ocean stress term does not dissipate KE but to the contrary is a source of KE; it clearly acts to set the ice in motion. Moreover, E_{oi} is generally much larger than the rate of KE input due to the wind in these regions (Figure 10b). These zones of positive E_{oi} in the T simulation are very well spatially correlated with zones of strongly negative E_r. This means that the ocean stress term in these tidally active regions increases the KE of the ice with a notable fraction of it being dissipated by the rheology term (by plastic deformations).

Following Koentopp et al. (2005), we use high-frequency outputs (hourly) to plot various time series at a point to gain further insight into the effect of the tides on the ice cover. This point is located in the Gulf of Boothia and is marked by a cross in the yellow region of Figure 1. The time series start on 20 October 2005 and ends up on 15 June 2006. Note that we also studied other points, in all four tidally active regions, where the number of months of landfast ice is clearly lower in T than in NT and we found qualitatively similar behaviors as what is described below for the point in the Gulf of Boothia.

Large wind stress events at the beginning of the period (October–November 2005) increase the KE at this point in both simulations (Figure 11a). This leads to strong losses of KE due to the ocean stress term (Figure 11b). Both simulations exhibit an active ice cover at this point (Figure 11d). Starting in December, the NT simulation is almost always at rest; it exhibits a few episodes with a small nonzero ice speed. The last one occurs at the end of January, and it is associated with a large wind stress event (Figure 11a). This is the same event indicated by the black arrow in Figure 5. After this strong wind event, the ice in the NT simulation is landfast at this point up until the end of our high-frequency record. In the T simulation, the same point is never landfast and exhibits an ice speed that is clearly related to the tidal forcing (semidiurnal, diurnal, and ~14-day spring-neap oscillation). From the end of November 2005 to the end of May 2006, the ocean stress term is always a source of KE at this point in the T simulation. Interestingly, while the wind stress in the NT simulation is either zero or a source of KE, the wind stress in the T simulation can be a source or lead to a loss
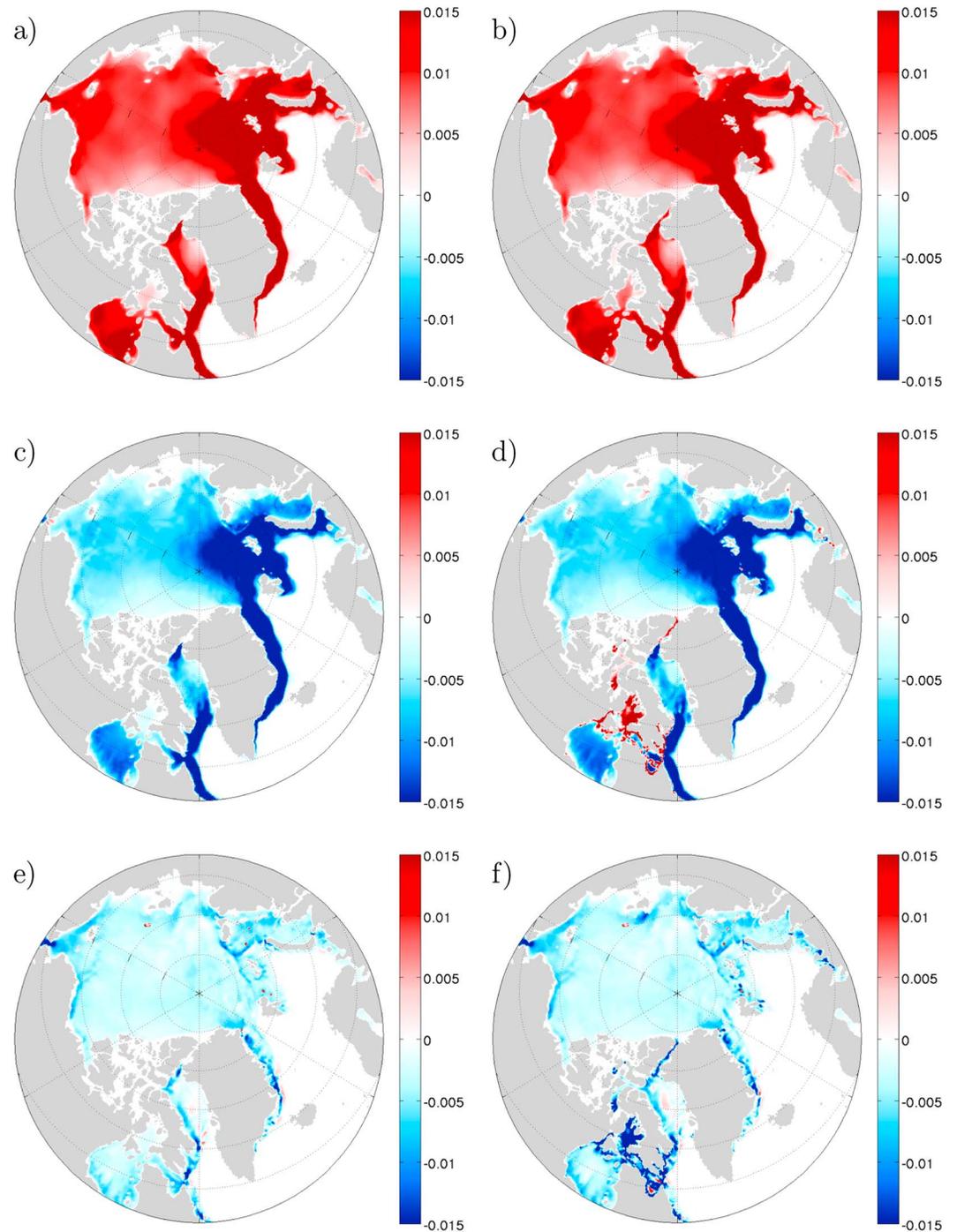
Figure 10. January–May 2006 mean (calculated from hourly outputs) rate of change of kinetic energy (KE) per unit area due to the atmospheric stress term (E_{ai}) for the NT simulation (a) and the T simulation (b). January–May 2006 mean (calculated from hourly outputs) rate of change of KE per unit area due to the ocean stress term (E_{oi}) for the NT simulation (c) and the T simulation (d). January–May 2006 mean (calculated from hourly outputs) rate of change of KE per unit area due to the rheology term (E_r) for the NT simulation (e) and the T simulation (f). Positive (negative) values in red (in blue) indicate that the term provides (removes) KE to the ice cover. The units for the six panels are W/m^2.
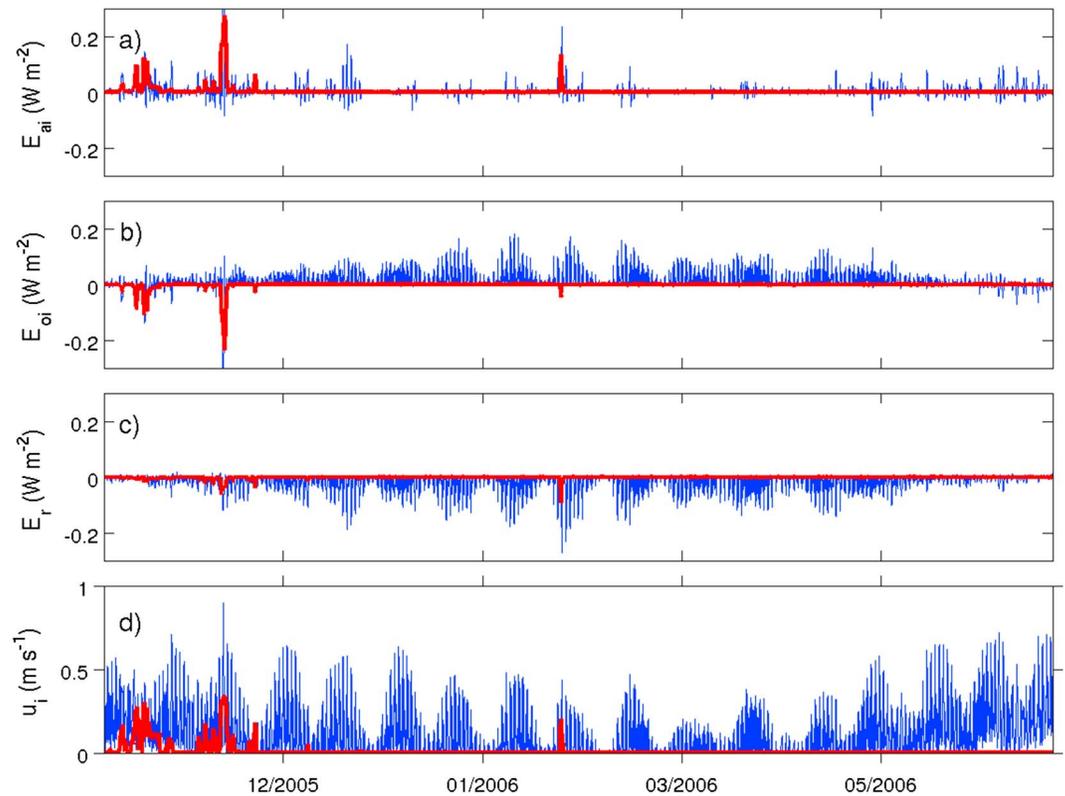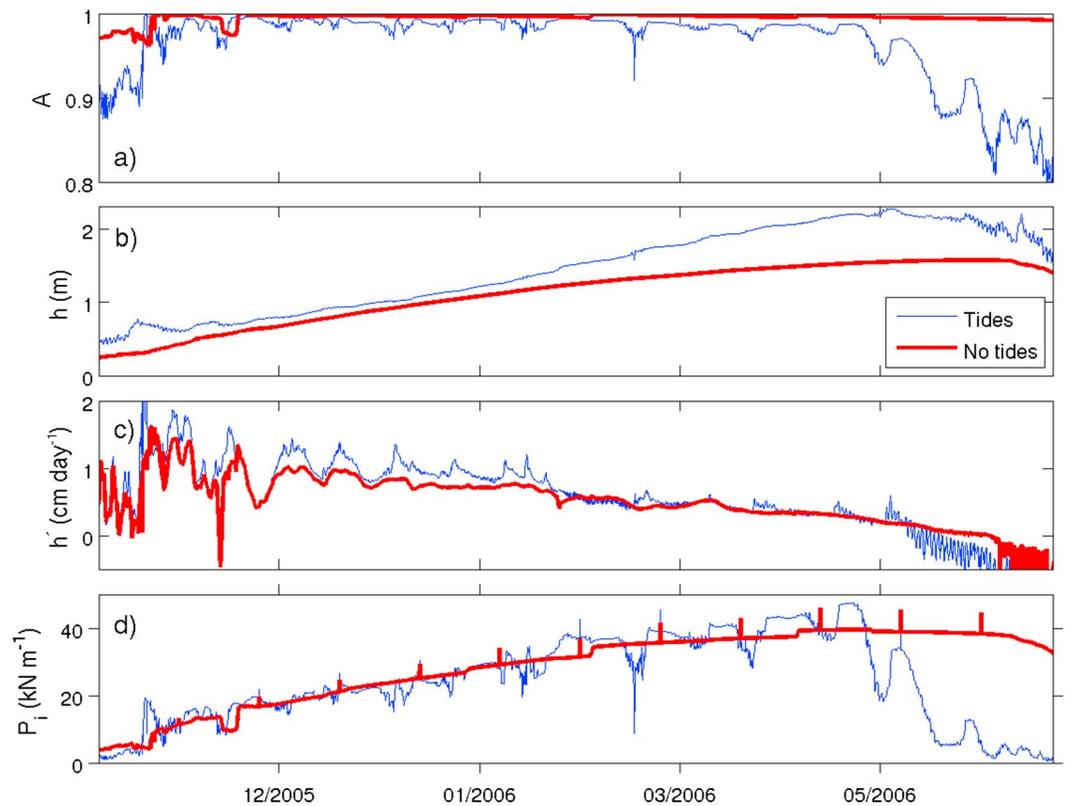
Figure 11. Time series at a point in the Gulf of Boothia of the rate of change of kinetic energy per unit area due the atmospheric stress (a), the ocean stress (b), and the rheology term (c) and time series of the ice speed (d). The NT simulation is in red, and the T one is in blue.

of KE (depending whether the wind is in the direction or in the opposite direction of the ice velocity vector). The rheology term dissipates quite a lot of KE in the T simulation except at the beginning and at the end of the period shown (because the ice strength is then very small; Figure 12d).

In the NT simulation, the ice concentration is close to 1 at the end of November 2005 and stays like this up until May 2006 (Figure 12a). In the time series for the T simulation, the ice concentration shows a lot more variability as the ice is still active. The more active and thicker ice in T than in NT (Figure 12b) suggests that there is more ice production in the T simulation than in the NT one. This is indeed the case as shown in Figure 12c. The ice strength (Figure 12d) in the T time series *oscillates around* the NT one. On average, the ice strengths are similar because the decrease due to the lower ice concentration in the T time series is compensated by a higher thickness. Even when there are episodes for which the ice strength in the T simulation is larger than in the NT one, the ice is not landfast due to the much larger ocean stress at the ice interface.

Another striking difference in the two time series is the behavior of the ice concentration, thickness, and melt in May 2006 (Figure 12). The ice concentration and thickness start to decrease at the beginning of May in T while this happens at the end of the month for the NT time series. This is likely a consequence of the ice-albedo feedback (more absorption of solar radiation) due to the already slightly lower concentration at the beginning of May and the more active ice cover and possibly larger ocean heat fluxes (this would require further investigation).

Temperature and salinity profiles at this location also help to understand the interactions between the ocean and the sea ice (Figure 13). At the beginning of the period on 20 October 2005, the vertical structure of the temperature and salinity profiles in T and the ones in NT are relatively similar as opposed to the profiles at the end of period. Indeed, the profiles on 3 May 2006 indicate there is a lot more vertical mixing in T than in NT. The fact that the warm layer below the mixed layer is eroded in T compared to NT (Figure 13a) suggests that there are larger vertical heat fluxes in T in winter at the ice underside, but that this is more than compensated by

Figure 12. Time series at a point in the Gulf of Boothia of the ice concentration (a), the ice thickness (b), the rate of change of h due to thermodynamic processes (i.e., $h' = \partial h / \partial t$ in cm/day; c), and the ice strength (d). The NT simulation is in red, and the T one is in blue.

increased heat loss to the atmosphere (consistent with more ice growth). The saltier mixed layer in T compared to NT could also be evidence of a greater ice production (due to salt rejection). These very different vertical profiles in T compared to NT could also (partly) be explained by the critical latitude effects of tides, which tend to create very thick surface mixed-layers and bottom boundary layers (Luneva et al., 2015). It is indeed interesting to notice the presence of a well mixed bottom layer in the T simulation that is present on the profiles of 20 October 2005 and 3 May 2006. A more complete understanding of the ocean vertical structure is beyond the scope of this paper and would require more investigation.
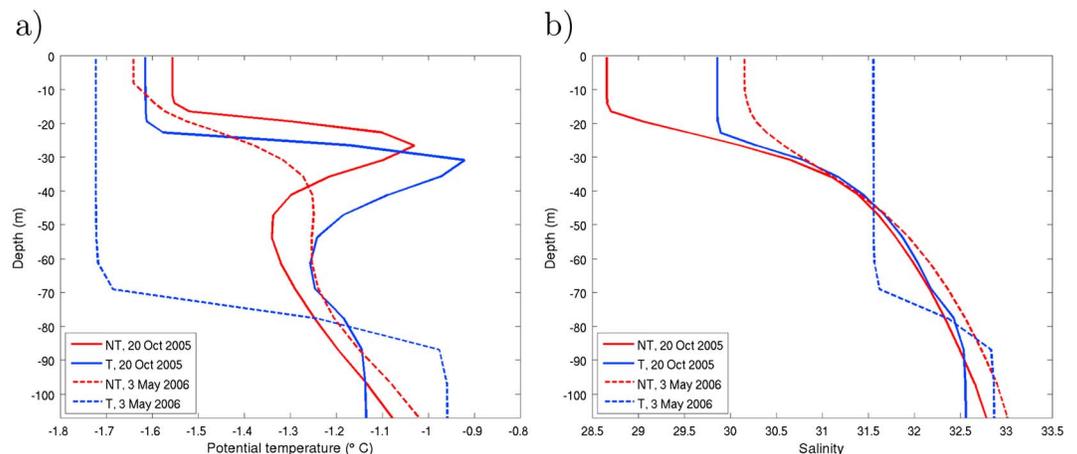
Figure 13. Ocean temperature (a) and salinity (b) profiles at a point in the Gulf of Boothia on 20 October 2005 (solid lines) and on 3 May 2006 (dashed lines) for the NT simulation (in red) and the T simulation (in blue).

6. Concluding Remarks

This paper addresses the following questions: (1) What is the impact of tides on the simulated landfast ice cover? (2) Which physical mechanisms are involved?

Using a 0.25° pan-Arctic ice-ocean model, a simulation without tides (NT) and a simulation with 13 tidal constituents (T) were conducted. When including the tides, the simulated landfast ice cover is strongly modified in tidally active regions; the area of simulated landfast ice is notably reduced and usually more in line with the observations. The most striking differences are found in the Gulf of Boothia, Prince Regent Inlet, Lancaster Sound, Foxe Basin, and in Nares Strait. The impact of tides on the landfast ice cover is mostly a local phenomenon; in regions with weak tidal forcing, the landfast ice cover in the T simulation is similar to the one in the NT simulation.

We demonstrate that the first-order mechanism responsible for the lower extent of landfast ice in tidally active regions is the much larger ocean-ice stress in the T simulation than in the NT one. While, on average (January–May), the ocean stress dissipates ice KE everywhere on the domain in the NT simulation, the situation is very different in tidally active regions in the T simulation. Indeed, in these regions, the ocean stress is usually a source of sea ice KE; the largest inputs of KE by the ocean stress are on average found in Foxe Basin, Gulf of Boothia, and Nares Strait. Moreover, in these regions, the rate of KE input is usually larger for the ocean stress term than for the wind stress. Also, in these regions, a notable fraction of the KE is dissipated by the sea ice rheology term (by plastic deformations). This is again a remarkable difference between the NT and T simulations.

These plastic deformations are characterized by a regular divergence-convergence (often with shear) cycle. On average (January–May) the ice concentration is lower in the T simulation than in the NT one in tidally active regions. These frequent openings in the sea ice cover lead to a higher production of new sea ice in the T simulation than in the NT one (mostly in Canadian waters). This is an indication that the lower extent of landfast ice in the T simulation compared to the NT one is not thermodynamically driven; the thicker ice in the T simulation should favor the formation/stabilization of a landfast ice cover.

In the simulations described here, constant atmospheric and oceanic neutral drag coefficients were used following the formulation of Roy et al. (2015). We speculate that the processes described above could even be more important if form drag (Tsamados et al., 2014) was also considered. Essentially, we argue that the tidally induced divergence-convergence cycle which leads to thicker ice in winter should increase the form drag and therefore further increase the ocean stress at the ice interface. This potential positive feedback mechanism would require to be investigated in an ice-ocean model that includes the effect of form drag.

Because the ice is usually thicker in tidally active regions in the T simulation than in the NT one, there is more grounding. However, this occurs over a few small regions (mostly in the southern part of the Gulf of Boothia and in the eastern part of Foxe Basin) as most channels and inlets are too deep for pressure ridges to reach the seafloor. In fact, in the CAA and in Nares Strait, grounding is not an important mechanism for the formation and stabilization of the landfast ice cover.

Although the simulation with tides leads to an overall better landfast ice cover than the NT experiment, the region of Barrow Strait is an exception. Indeed, compared to observations, the region free of landfast ice in this section of the Northwest passage extends too far west. Another interesting point about our simulations is the change in the landfast ice conditions in Nares Strait. In the NT simulation, the average number of months of landfast indicate there is an ice bridge that sometimes form in Nares Strait while the ice bridge does not exist in the T simulation. Compared to the observations, the NT simulation overestimates the number of months of landfast ice while it is the opposite for the simulation with tides (recall that, in Nares Strait, the amplitudes of our simulated tides are overestimated compared to the reconstructed OSU tides; Figure 3). These results suggest that some models (e.g., Dansereau et al., 2017) might be able to simulate the North Water Polynya ice bridge and landfast ice in some regions of the CAA due to a compensation of errors; the ice is too thin or too weak but the model still simulates landfast ice because tidal forcing is not considered.

To further improve the simulation of landfast ice, we are currently developing more sophisticated grounding and seabed stress formulations that depend on the ice thickness distribution. Moreover, in this framework, the seafloor is not considered to be flat but is rather expressed based on a probability distribution. As future work,

we also plan to study the influence of landfast ice, tides, and mixing in the CAA on the export of freshwater to subpolar convective regions.

References

Årthun, M., Ingvaldsen, R., Smedsrud, L., & Schrum, C. (2011). Dense water formation and circulation in the Barenas Sea. *Deep Sea Research Part I: Oceanographic Research Papers*, *58*(8), 801–817. https://doi.org/10.1016/j.dsr.2011.06.001

Bouchat, A., & Tremblay, B. (2014). Energy dissipation in viscous-plastic sea-ice models. *Journal of Geophysical Research: Oceans*, *119*, 976–994. https://doi.org/10.1002/2013JC009436

Dansereau, V., Weiss, J., Saramito, P., Lattes, P., & Coche, E. (2017). Ice bridges and ridges in the Maxwell-EB sea ice rheology. *The Cryosphere*, *11*(5), 2033–2058. https://doi.org/10.5194/tc-11-2033-2017

Dethleff, D., Loewe, P., & Kleine, E. (1998). The Laptev Sea flaw lead-detailed investigation on ice formation and export during 1991/1992 winter season. *Cold Regions Science and Technology*, *27*, 225–243.

Divine, D. V., Korsnes, R., Makshtas, A. P., Godtliebsen, F., & Svendsen, H. (2005). Atmospheric-driven state transfer of shore-fast ice in the northeastern Kara Sea. *Journal of Geophysical Research*, *110*, C09013. https://doi.org/10.1029/2004JC002706

Dumont, D., Gratton, Y., & Arbetter, T. E. (2009). Modeling the dynamics of the North Water polynya ice bridge. *Journal of Physical Oceanography*, *39*, 1448–1461. https://doi.org/10.1175/2008JPO3965.1

Egbert, G. D., & Erofeeva, S. Y. (2002). Efficient inverse modeling of barotropic ocean tides. *Journal of Atmospheric and Oceanic Technology*, *19.2*, 183–204.

Flather, R. A. (1976). A tidal model of the northwest European continental shelf. *Memoires de la Societe Royale des Sciences de Liege*, *10*, 141–164.

Garric, G., Parent, L., Greiner, E., Drévillon, M., Hamon, M., Lellouche, J.-M., et al. (2017). Performance and quality assessment of the global ocean eddy-permitting physical reanalysis GLORYS2V4. In *EGU General Assembly Conference Abstracts, EGU General Assembly Conference Abstracts*, pp. 18776. vol. 19.

Haas, C., Dierking, W., Busche, T., & Hoelemann, J. (2005). ENVISAT ASAR monitoring of polynya processes and sea ice production in the Laptev Sea (*Tech. rep.*) Salzburg: Alfred Wegener Institute.

Hannah, C., Dupont, F., & Dunphy, M. (2009). Polynyas and tidal currents in the Canadian Arctic Archipelago. *Arctic*, *62*, 83–95.

Hibler, W. D. (1979). A dynamic thermodynamic sea ice model. *Journal of Physical Oceanography*, *9*, 815–846.

Holloway, G., & Proshutinsky, A. (2007). Role of tides in arctic ocean/ice climate. *Journal of Geophysical Research*, *112*, C04S06. https://doi.org/10.1029/2006JC003643

Hunke, E. C. (2001). Viscous-plastic sea ice dynamics with the EVP model: Linearization issues. *Journal of Computational Physics*, *170*, 18–38.

Hunke, E. C., & Lipscomb, W. H. (2008). CICE: The Los Alamos sea ice model. Documentation and software user's manual version 4.0 (*Tech. Rep. LA-CC-06-012*). Los Alamos, NM: Los Alamos National Laboratory.

Itkin, P., Losch, M., & Gerdes, R. (2015). Landfast ice affects the stability of the Arctic halocline: Evidence from a numerical model. *Journal of Geophysical Research: Oceans*, *120*, 2622–2635. https://doi.org/10.1002/2014JC010353

Johnson, M., Proshutinsky, A., Aksenov, Y., Nguyen, A. T., Lindsay, R., Haas, C., et al. (2012). Evaluation of Arctic sea ice thickness simulated by Arctic Ocean Model Intercomparion Project models. *Journal of Geophysical Research*, *117*, C00D13. https://doi.org/10.1029/2011JC007257

Koentopp, M., Eisen, O., Kottmeier, C., Padman, L., & Lemke, P. (2005). Influence of tides on sea ice in the Weddell Sea: Investigations with a high-resolution dynamic-thermodynamic sea ice model. *Journal of Geophysical Research*, *110*, C02014. https://doi.org/10.1029/2004JC002405

König Beatty, C., & Holland, D. M. (2010). Modeling landfast sea ice by adding tensile strength. *Journal of Physical Oceanography*, *40*, 185–198. https://doi.org/10.1175/2009JPO4105.1

Kowalik, Z., & Proshutinsky, A. Y. (1994). The Arctic Ocean tides. In *The Polar Oceans and their role in shaping the global environment* (Vol. 85, pp. 137–158). Washington, DC: American Geophysical Union.

Laliberté, F., Howell, S. E. L., Lemieux, J.-F., Lei, J., & Dupont, F. (2018). What historical landfast ice observations tell us about projected ice conditions in arctic archipelagoes and marginal seas under anthropogenic forcing. *The Cryosphere*. https://doi.org/10.5194/tc-2018-24

Lemieux, J.-F., Dupont, F., Blain, P., Roy, F., Smith, G. C., & Flato, G. M. (2016). Improving the simulation of landfast ice by combining tensile strength and a parameterization for grounded ridges. *Journal of Geophysical Research: Oceans*, *121*, 7354–7368. https://doi.org/10.1002/2016JC012006

Lemieux, J.-F., Tremblay, L. B., Dupont, F., Plante, M., Smith, G. C., & Dumont, D. (2015). A basal stress parameterization for modeling landfast ice. *Journal of Geophysical Research: Oceans*, *120*, 3157–3173. https://doi.org/10.1002/2014JC010678

Lieser, J. L. (2004). A numerical model for short-term sea ice forecasting in the Arctic (PhD thesis), Universitat Bremen, Germany.

Lipscomb, W. H., Hunke, E. C., Maslowski, W., & Jakacki, J. (2007). Ridging, strength, and stability in high-resolution sea ice models. *Journal of Geophysical Research*, *112*, C03S91. https://doi.org/10.1029/2005JC003355

Locarnini, R. A., Mishonov, A. V., Antonov, J. I., Boyer, T. P., Garcia, H. E., Baranova, O. K., et al. (2013). World ocean Atlas 2013, volume 1: Temperature In S. Levitus (Ed.), A. Mishonov (Ed.), NOAA Atlas NESDIS 73 (40 pp.).

Luneva, M. V., Aksenov, Y., Harle, J. D., & Holt, J. T. (2015). The effect of tides on the water mass mixing and sea ice in the Arctic Ocean. *Journal of Geophysical Research: Oceans*, *120*, 6669–6699. https://doi.org/10.1002/2014JC010310

Madec, G. (2008). *NEMO ocean engine*. France: Note du Pôle de modélisation, Institut Pierre-Simon Laplace (IPSL). No 27, ISSN No 1288-1619.

Mahoney, A. R., Eicken, H., Gaylord, A. G., & Gens, R. (2014). Landfast sea ice extent in the Chukchi and Beaufort Seas: The annual cycle and decadal variability. *Cold Regions Science and Technology*, *103*, 41–56. https://doi.org/10.1016/j.coldregions.2014.03.003

Mahoney, A., Eicken, H., & Shapiro, L. (2007). How fast is landfast sea ice? A study of the attachment and detachment of nearshore ice at Barrow, Alaska. *Cold Regions Science and Technology*, *47*, 233–255. https://doi.org/10.1016/j.coldregions.2006.09.005

Megann, A., Storkey, D., Aksenov, Y., Alderson, S., Calvert, D., Graham, T., et al. (2014). GO5.0: The joint NERC-Met Office NEMO global ocean model for use in coupled and forced applications. *Geoscientific Model Development*, *7*, 1069–1092. https://doi.org/10.5194/gmd-7-1069-2014

National Ice Center (2006, updated 2009). *National Ice Center Arctic Sea Ice Charts and Climatologies in Gridded Format*. In F. Fetterer, & C. Fowley. Boulder, CO: National Snow and Ice Data Center. https://doi.org/10.7265/N5X34VDB. Retrieved from http://nsidc.org/data/g02172

Nihashi, S., & Ohshima, K. I. (2015). Circumpolar mapping of Antarctic coastal polynyas and landfast sea ice: Relationship and variability. *Journal of Climate*, *28*(9), 3650–3670. https://doi.org/10.1175/JCLI-D-14-00369.1

Olason, E. (2016). A dynamical model of Kara Sea land-fast ice. *Journal of Geophysical Research: Oceans*, *121*, 3141–3158. https://doi.org/10.1002/2016JC011638

Rabe, B., Johnson, H. L., Münchow, A., & Melling, H. (2012). Geostrophic ocean currents and freshwater fluxes across the Canadian polar shelf via Nares Strait. *Journal of Marine Research*, *70*, 603–640. https://doi.org/10.1357/002224012805262725

Rallabandi, B., Zheng, Z., Winton, M., & Stone, H. A. (2017). Formation of sea ice bridges in narrow straits in response to wind and water stresses. *Journal of Geophysical Research: Oceans*, *122*, 5588–5610. https://doi.org/10.1002/2017JC012822

Rippeth, T. P., Lincoln, B. J., Lenn, Y.-D., Green, J. A. M., Sundfjord, A., & Bacon, S. (2015). Tide-mediated warming of Aarctic halocline by Atlantic heat fluxes over rough topography. *Nature Geoscience*, *8*, 191–944.

Rothrock, D. A. (1975). The energetics of the plastic deformation of pack ice by ridging. *Journal of Geophysical Research*, *80*(33), 4514–4519.

Roy, F., Chevallier, M., Smith, G. C., Dupont, F., Garric, G., Lemieux, J.-F., et al. (2015). Arctic sea ice and freshwater sensitivity to the treatment of the atmosphere-ice-ocean surface layer. *Journal of Geophysical Research: Oceans*, *120*, 4392–4417. https://doi.org/10.1002/2014JC010677

Schweiger, A., Lindsay, R., Zhang, J., Steele, M., & Stern, H. (2011). Uncertainty in modeled Arctic sea ice volume. *Journal of Geophysical Research*, *116*, C00D06. https://doi.org/10.1029/2011JC007084

Selyuzhenok, V., Mahoney, A. R., Krumpen, T., Castellani, G., & Gerdes, R. (2017). Mechanisms of fast-ice development in the southeastern Laptev Sea: A case study for winter of 2007/08 and 2009/10. *Polar Research*, *36*, 1411140. https://doi.org/10.1080/17518369.2017.1411140

Serson, H. V. (1974). Sverdrup channel (*Tech. rep.*) Canada: Department of National Defence. Defence Research Establishment Ottawa., (DREO Tech. Note 72-6).

Smith, G. C., Roy, F., Mann, P., Dupont, F., Brasnett, B., Lemieux, J.-F., et al. (2014). A new atmospheric dataset for forcing ice-ocean models: Evaluation of reforecasts using the Canadian global deterministic prediction system. *Quarterly Journal of the Royal Meteorological Society*, *140*(680), 881–894. https://doi.org/10.1002/qj.2194

Smith, G. C., Roy, F., Reszka, M., Surcel Colan, D., He, Z., Deacu, D., et al. (2016). Sea ice forecast verification in the Canadian global ice ocean prediction esteem. *Quarterly Journal of the Royal Meteorological Society*, *142*(695), 659–671. https://doi.org/10.1002/qj.2555

Tsamados, M., Feltham, D. L., Schroeder, D., & Flocco, D. (2014). Impact of variable atmospheric and oceanic form drag on simulations of Arctic sea ice. *Journal of Physical Oceanography*, *44*, 1329–1353. https://doi.org/10.1175/JPO-D-13-0215.1

Ungermann, M., Tremblay, L. B., Martin, T., & Losch, M. (2017). Impact of the ice strength formulation on the performance of a sea ice thickness distribution model in the Arctic. *Journal of Geophysical Research: Oceans*, *122*, 2090–2107. https://doi.org/10.1002/2016JC012128

Yu, Y., Stern, H., Fowler, C., Fetterer, F., & Maslanik, J. (2014). Interannual variability of Arctic landfast ice between 1976 and 2007. *Journal of Climate*, *27*, 227–243. https://doi.org/10.1175/JCLI-D-13-00178.1

Zhang, J., & Rothrock, D. A. (2003). Modeling global sea ice with a thickness and enthalpy distribution model in generalized curvilinear coordinates. *Monthly Weather Review*, *131*(5), 681–697.

Zweng, M. M., Reagan, J. R., Antonov, J. I., Locarnini, R. A., Mishonov, A. V., Boyer, T. P., et al. (2013). World Ocean Atlas 2013, Volume 2: Salinity. In S. Levitus (Ed.), A. Mishonov Technical Ed., NOAA Atlas NESDIS 74 (39 pp.).